Quarterly Report for
Contract DE-FG36-02ID14418
Stanford Geothermal Program
January-March 2004

Table of Contents

1. STEAM AND WATER RELATIVE PERMEABILITIES FROM FIELD PRODUCTION DATA, AND LABORATORY VERIFICATION

This project is being conducted by Research Assistants Chih-Ying Chen and Jericho Reyes, Senior Research Engineer Kewen Li and Professor Roland Horne. In this research, the steam and water relative permeabilities at The Geysers and Salton Sea geothermal reservoirs were calculated from available production data. A method was used to estimate the relative permeability curves using Darcy's law from mass production rates of steam and water that are available from the DOGGR database. A verification was also conducted using data measured in laboratory steam-water flow experiments. The laboratory results show good agreement with the relative permeabilities calculated from a standard Darcy's Law approach. The water saturation estimated from the production data (i.e. the *flowing* water saturation) was found to be a significant underestimate compared to the in-place (*static*) saturation. From the laboratory experiments, the relationship between the flowing water saturation and the in-place water saturation was developed. The relative permeability curves inferred from field production data, corrected to static saturation, show a behavior that is very similar to that seen in laboratory experiments.

1.1 INTRODUCTION

There are two types of geothermal reservoirs: the vapor-dominated reservoir where steam is the principal recovery fluid and the liquid-dominated reservoir where liquid water is the principal recovery fluid. In both cases, the interaction between these two different phases has been the subject of numerous studies. Many measurements have encountered experimental difficulty due to the phase changes during the flow. An alternative way of determining how these two phases interact while in a state of flow would be very useful in the prediction of the ultimate recovery of the resource. Quantifying this interaction, by calculating the relative permeability of each of the phases, is of particular importance.

The objective of this study was to develop a method to calculate the relative permeabilities of steam and water by using production data from active geothermal fields, and to verify and calibrate this method using data from laboratory experiment. Knowledge of the relative permeabilities of steam and water will provide better understanding of the fluid flow interactions in the geothermal reservoir, and this is valuable in estimating the performance of a geothermal field and its capacity for further exploitation.

1.2 BACKGROUND

There have been numerous attempts to characterize the steam and water relative permeability curves both experimentally and theoretically. The main difficulty of direct measurement has been the phase changes that occur during steam and water multiphase flow. A number of experiments have been made in nonboiling flow in fractured media, such as in air-water (Diomampo, 2001) and water-oil. Current research on steam-water relative permeability in fractures (Chen *et al*. 2002, 2003) gives us a preliminary insight on the characteristics of the interaction of these two phases with one another.

The two frequently used functions for relative permeability are the linear model (X-curve) and the Corey-model (Corey, 1954). These functions are dependent on phase saturation. The X-curve has a linear relationship with saturation:

$$k_{rl} = S_l \tag{1.1}$$

$$k_{rg} = S_g \tag{1.2}$$

where S_l and S_g are the liquid and gas saturation respectively. The Corey model is expressed as follows :

$$k_{rl} = S^{*4} \tag{1.3}$$

$$k_{rg} = (1 - S^*)^2 (1 - S^{*2}) \tag{1.4}$$

$$S^* = (S_l - S_{rl})/(1 - S_{rl} - S_{rg}) \tag{1.5}$$

Chen et al. (2002) developed a method to compare steam- and air-water transport through fractured media. The main finding was that steam-water flow behavior in fractures is different from that of nitrogen-water flow. Chen et al. (2003) found less phase interference in steam-water flow, and saw the behavior of the steam-water relative permeabilities behave closer to the X-curve.

The DOGGR Database has been made available publicly by the California Division of Oil, Gas and Geothermal Resources. The database contains production histories of, among others, the Geysers and Salton Sea geothermal wells. The data include temperature, pressure and steam and water production rates, and these parameters were used here in this study. The Geysers Geothermal Field, a vapor-dominated reservoir field, is located in Northern California about 130 km north of San Francisco. The Salton Sea Geothermal Field, a liquid-dominated reservoir field, is located in Imperial County in Southern California.

1.3 METHOD

Shinohara (1978) described a method to estimate the steam and water relative permeabilities in geothermal reservoirs, and applied this method to production data from the Wairakei geothermal field in New Zealand. This method is simple and useful, in that it only needs the production flow rate history and the temperature of the reservoir, as well as the ability to evaluate each well separately. Some of the assumptions of this method include:

(1)   The pressure gradient is constant for a short time in each well.
(2)   The product of permeability and flowing area is constant in each well.

(3)   Fluid flow follows Darcy's Law.

Under these assumptions and from Darcy's law:

$$Q_w = \rho_w \frac{k}{\mu_w} k_{rw} Ap' \qquad (1.6)$$

$$Q_s = \rho_s \frac{k}{\mu_s} k_{rs} Ap' \qquad (1.7)$$

where Q is the mass flow rate, ρ is the density, μ is the dynamic viscosity, k_r is the relative permeability, k is the absolute permeability of the geothermal rock, A is the cross sectional area of flow, and p' is the pressure gradient. The subtitles w and s refer to water and steam respectively.

Dividing Equation 1.6 by Equation 1.7 gives us:

$$\frac{Q_w}{Q_s} = \frac{\upsilon_s}{\upsilon_w} \frac{k_{rw}}{k_{rs}} \qquad (1.8)$$

where υ is the kinematic viscosity.

Taking the sum of Equations 1.6 and 1.7 gives us:

$$Q = Q_w + Q_s = \left(\rho_w \frac{k_{rw}}{\mu_w} + \rho_s \frac{k_{rs}}{\mu_s} \right) kAp' = \left(\frac{k_{rs}}{\upsilon_s} \right) \left[1 + \left(\frac{Q_w}{Q_s} \right) \right] kAp' \qquad (1.9)$$

where Q is the total of mass production rate of steam and water.

If we assume kAp' is constant in each well, then Equation 1.9 shows that a plot of Q vs Q_w/Q_s would be almost linear when Q_w/Q_s is small, and we can find the value of kAp' from either the intercept or the gradient of the line on the graph. This intercept, where $Q_w/Q_s = 0$, becomes Q^*, where:

$$Q^* = \frac{1}{\upsilon_s} kAp' \qquad (1.10)$$

Because $k_{rs} = 1$ at $Q_w = 0$, then, substituting Equation 1.10 into Equation 1.6 and 1.7,

$$k_{rw} = \left(\frac{\upsilon_w}{\upsilon_s}\right)\left(\frac{Q_w}{Q*}\right) \tag{1.11}$$

$$k_{rs} = \frac{Q_s}{Q*} \tag{1.12}$$

Therefore knowing $Q*$, we can calculate k_{rs} and k_{rw} by also knowing Q_w, Q_s, υ_s, and υ_w Unfortunately, the actual water saturation cannot be obtained in actual geothermal reservoirs. To estimate water saturation roughly using the production data only, the volumetric ratios can be used to infer the reservoir water saturation in the absence of residual saturation and for homogeneous flow of both phases. This estimated water saturation is called the *flowing* water saturation, and can be calculated from:

$$S_{w,f} = \frac{(1-x)V_w}{(1-x)V_w + xV_w} \tag{1.13}$$

where x is the mass fraction of steam and v_w and v_s is the specific volume of water and steam, respectively. This flowing saturation is often referred to as the *fractional flow*. It must be understood that the flowing saturation is different from the actual (in-place) saturation in a geothermal reservoir.

In the next section, we will describe the application of Shinohara's method to the production data from The Geysers and Salton Sea geothermal fields. After that, we will present a verification of Shinohara's method by applying it to laboratory data in which the steam-water relative permeabilities were already known. Comparison with the laboratory data also reveals the relationship between the flowing saturation and the actual (in-place) saturation.

1.4 RESERVOIR APPLICATIONS

The production data in the Geysers and Salton Sea geothermal fields include temperature, pressure and steam and water production rates. In choosing the wells to be used in this study, a number of issues had to be addressed. First, for the vapor-dominated reservoir, we had to find data from wells that had both steam and water production. Of the 503 wells made available to us from The Geysers, 25 of them produced water. Nine wells were ultimately used, as these wells had a sufficient number of readings for the calculation. Also, the first assumption of Shinohara's method tells us that it is necessary to choose a short time period over which we can assume a constant pressure gradient. Since production data are usually intermittent in nature and often have periodic fluctuations, we had to find data sets that had significant stable periods. Of the 128 wells documented in the database that belong to the Salton Sea field operated by CalEnergy, we used six wells for our liquid-dominated case.

Figures 1.1 and 1.2 are examples of steam and water production histories from Coleman 4-5, a Geysers well, and IDD – 9, a well from the Salton Sea geothermal field. Well IDD-9 (Figure 1.2) from Salton Sea had zero production for much of its history. We chose an interval that we can assume to have a roughly constant pressure gradient. For this work we chose an interval from mid-1990 to late-1992. Choosing the time interval for the vapor-dominated well is much easier. We tried to omit extreme readings from our analysis, therefore the spike seen in 1986-1987 was not chosen as part of the range. For this work, we used a data interval from mid-1987 to 1989. Figures 1.3 and 1.4 show the Q vs Q_w/Q_s graphs for Coleman 5-5 and IDD – 9, respectively. The value of $Q*$ is inferred from the y-intercept value from the linear fit to the graph. Table 1.1 shows the $Q*$ inferred from all the wells used in the study.
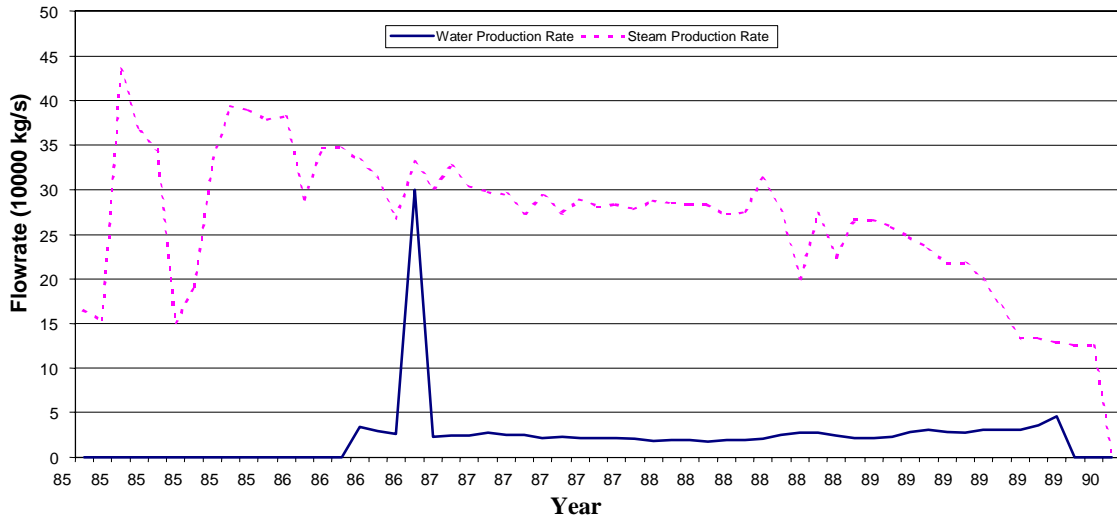

Figure 1.1: Steam and Water Production History of Coleman 4-5, The Geysers Geothermal Field.
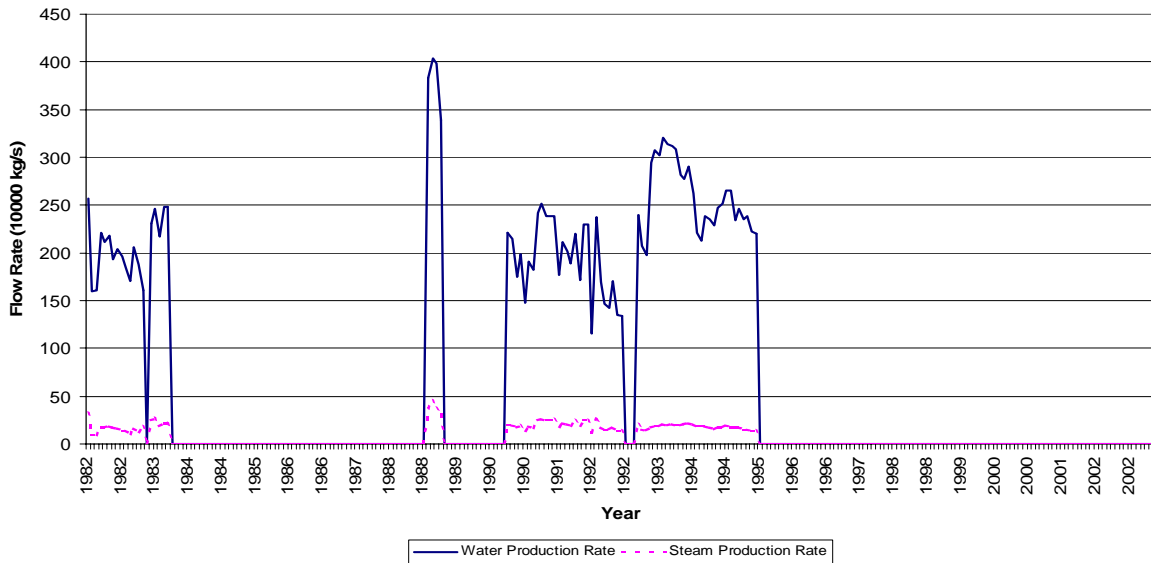

Figure 1.2: Steam and Water Production History of IID - 9, Salton Sea Geothermal Field.
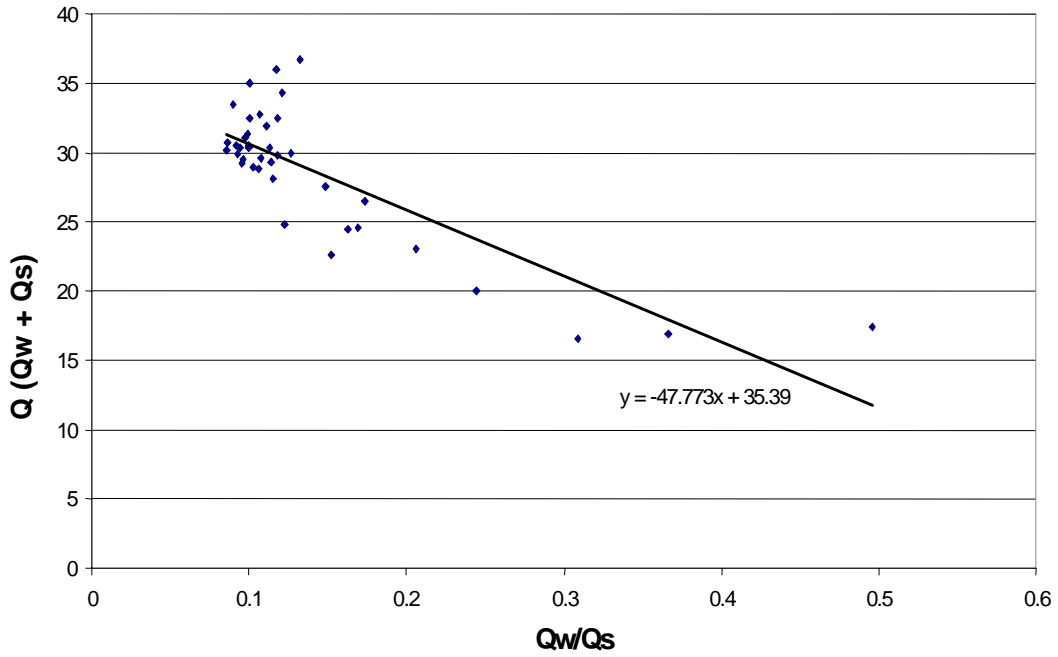
5

Figure 1.3: Q vs. Qw/Qs to infer Q* for Coleman 4-5, The Geysers Geothermal Field.
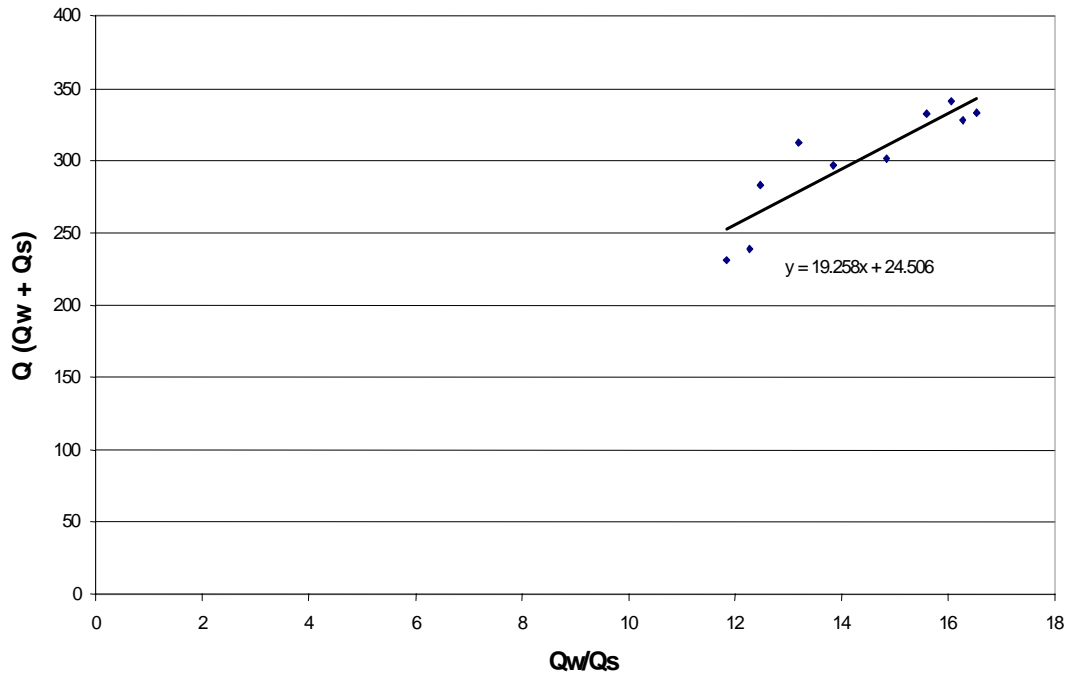

Figure 1.4: Q vs. Qw/Qs to infer Q* for IID - 9, Salton Sea Geothermal Field.

Table 1.1: Inferred Q* values for the Geysers and Salton Sea Geothermal Field Wells.

Geysers Wells	Q*	Salton Sea Wells	Q*
Coleman 4-5	35.39	IID – 9	100
Coleman 5-5	35.649	Sinclair 20	75
Coleman 3-5	24.186	Vonderahe 1	437.56
Francisco 2-5	24.182	Sinclair 10	298.62
Coleman 1A-5	24.09	Elmore 100	200
Thorne 6	33.59	Sinclair 11	256.5
Thorne 1	17.384		
Francisco 5-5	23.52		
CA-5636 6.8E-20	27.868		

If we compare the Q^* values between The Geysers wells and the Salton Sea wells, we can see that The Geysers' Q^* values are smaller than those in the Salton Sea. Also, The Geysers' Q^* values are close to each other. This is an extension of the second assumption made by Shinohara in developing his method. Not only is kAp' constant in a well, wells that are near each other or belong to the same geothermal field also have similar kAp' values. Since the wells in a certain geothermal field mainly have the same k values, and to a certain extent, A and p', then our inferred values are consistent with each other. The Salton Sea wells have a wider range of values of Q*, but are generally of the same magnitude and larger than those in The Geysers. To evaluate the kinematic viscosities and mass production rates of the steam and water correctly, we must infer the bottomhole conditions, as these reflect the true flowing conditions of the well. We made temperature corrections based on the documented depths of the wells.

We can now use Equations 1.11 and 1.12 to calculate the relative permeabilities of steam and water. Figures 1.5 and 1.6 shows us a plot of relative permeability with water saturation for The Geysers and Salton Sea geothermal wells, respectively. Note that these graphs are plotted against the *flowing* saturation, $S_{w,f}$, as defined by Equation 1.13. The *flowing* saturation excludes the immobile water and steam fractions. Th water saturation was estimated by using Equation 1.13 since the actual (in-place) water saturation was not available. Figure 1.5 shows The Geysers relative permeability plot. Because The Geysers is a vapor-dominated reservoir, we expected the low water saturation values. Figure 1.6, the Salton Sea examples, shows us a larger range for flowing water saturation, with a maximum at around 0.25. Even with a vapor-dominated reservoir, we see that, volumetrically, the steam saturation values still dominate, even if, by mass, water production is greater. We can see the general trend of the relative permeability curves by plotting both well samples into Figure 1.7. From Figure 1.7, we see that the relative permeability values for the vapor-dominated and liquid-dominated samples are only partially consistent with each other. For the relative permeability of steam, The Geysers calculation gives us a sharp drop in k_{rs} at small values of $S_{w,f}$. We then see a plateau of values approaching $S_{w,f} = 0.1$ from the Salton Sea values. For the relative permeability of water, we see a more constant and stable rise as the water saturation increases. The steepness of the rise for both sets of well samples is consistent. The water saturation in the

figures seem to be much smaller than the traditional behavior of relative permeability curves, because of the use of flowing saturation based on Equation 1.13, rather than the true in-place saturation. A mapping between flowing and static water saturations based on laboratory experiment will be address in the next section.
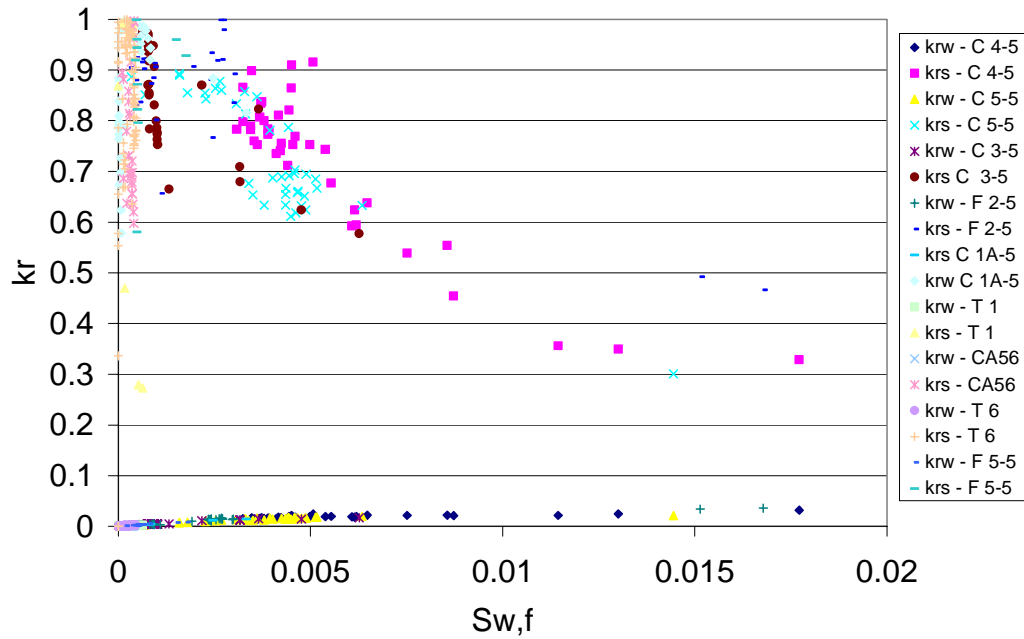

Figure 1.5: Plot of relative permeability curves against flowing water saturation for The Geysers Geothermal Field.
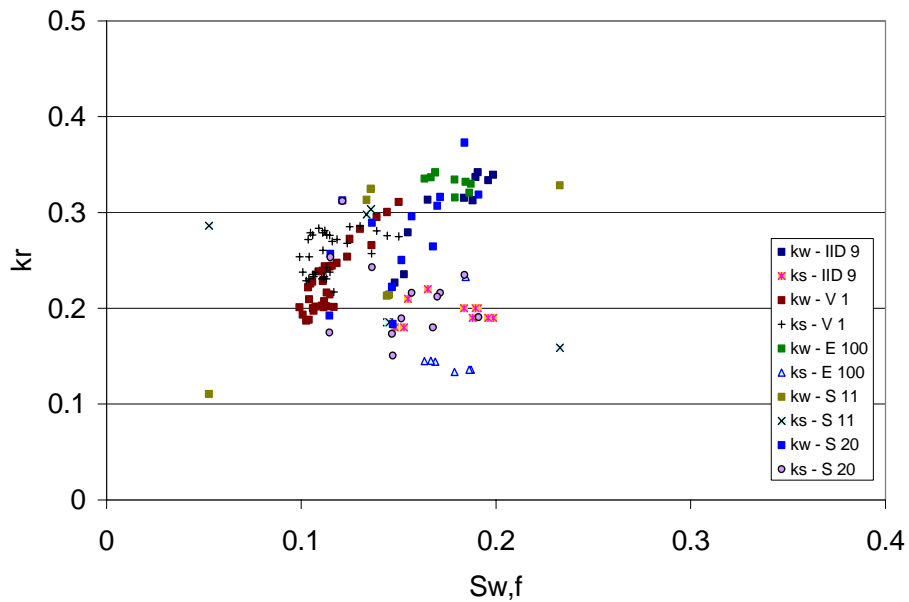

Figure 1.6: Plot of relative permeability curves against water saturation for the Salton Sea Geothermal Field.
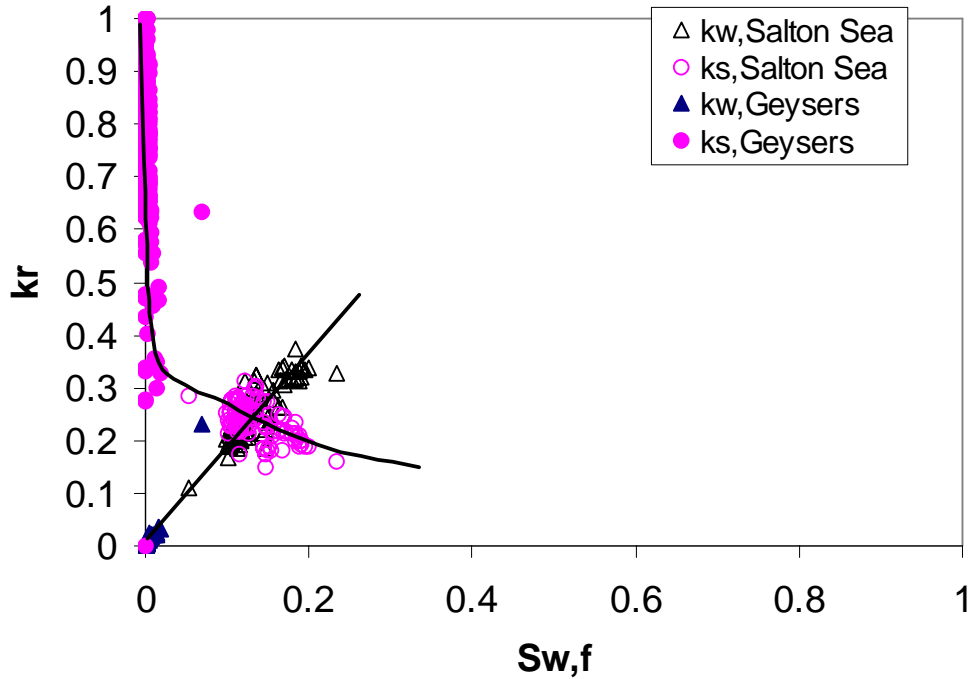
Figure 1.7: Plot of relative permeability curves against water saturation for The Geysers and Salton Sea Geothermal Reservoir Fields.

To compare the estimated relative permeability values with the two most commonly assumed models of relative permeabilities, namely Corey and X curves, we plot the computed k_{rw} and k_{rs} values with these model curves in Figure 1.8. For The Geysers samples, we see that the relative permeability follows the Corey-model. On the other hand, the Salton Sea values lie more in the region between the X-curve and Corey-curve.
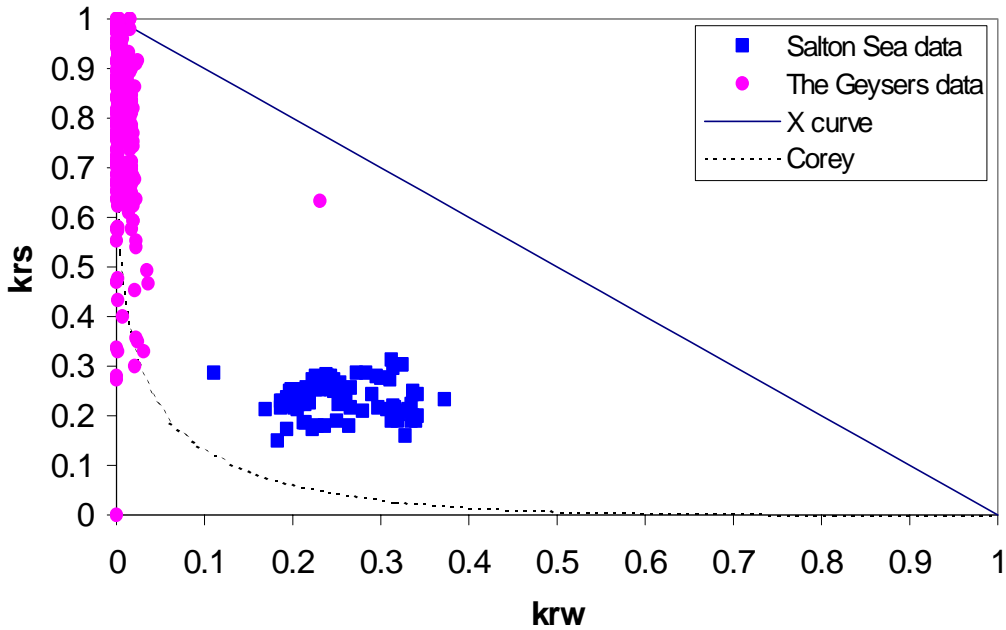

Figure 1.8: Plot of k_{rw} vs k_{rs} for The Geysers and Salton Sea Geothermal Field, with the Corey and X-curves.

9

We plot the data from Figure 1.8 again, this time with logarithmic axes, in Figure 1.9. We see from this graph that the calculated values lie between the X- and Corey-curves, for both The Geysers and Salton Sea wells.
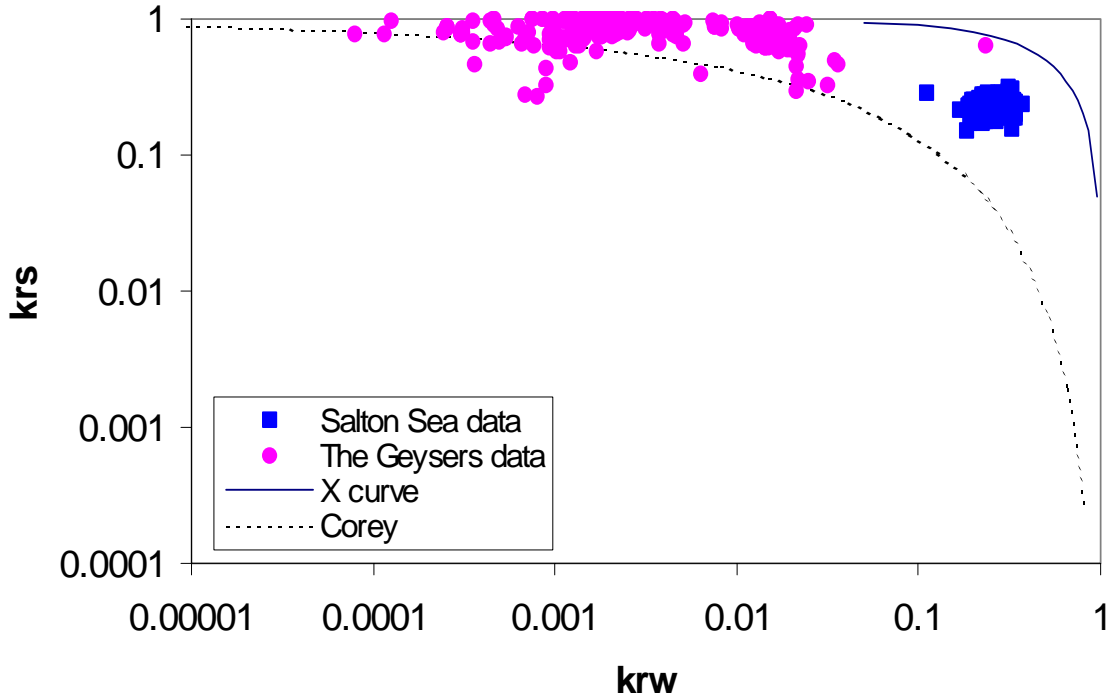

Figure 1.9: Logarithmic Plot of k_{rw} vs k_{rs} for The Geysers and Salton Sea Geothermal Field, with the Corey and X-curves.

1.5 LABORATORY VERIFICATION

To confirm Shinohara's method and examine the relationship between the *flowing* saturation and the actual in-place (*static*) saturation, data from laboratory experiments were used. These data were obtained from steam-water flow experiments conducted by Chen *et al*. (2003). In these experiments, a FFRD (fractional flow ratio detector) device was used to sense both steam and water production rates. Flow visualization and image processing techniques were used to determine the water saturation (static), and differential pressure transducers were used to measure the pressure drop through the artificial reservoir (a single fracture). We used this "production data" from the laboratory to estimate relative permeabilities using Shinohara's method, and compared the results with those from the standard porous media approach provided by Chen *et al*. (2003).

Since the pressure gradient in the laboratory scale experiment was not constant, we scaled the data to a constant pressure gradient prior to the calculations. Figure 1.10 shows the Q vs. Q_w/Q_s plot in the experiment. The value of Q^* is 0.0032 ml/sec in this case. The steam-water relative permeabilities calculated from Shinohara's method (Equations 1.11 and 1.12) were compared with those from the porous media approach (1. 6 and 1.7). A close agreement of relative permeability values from these two methods is shown in Figure 1.11.

10

The steam-phase and water-phase values show less than 5% relative error between the two methods.

The relationship between flowing and static water saturations was examined by comparing the actual (static) water saturation measured in the experiment with the flowing water saturation calculated from Equation 1.13. From Figure 1.12, it is evident that the flowing water saturation is significantly less than the actual water saturation. The relationship between the two saturations can be expressed by a logarithmic trend as shown in Figure 1.13.
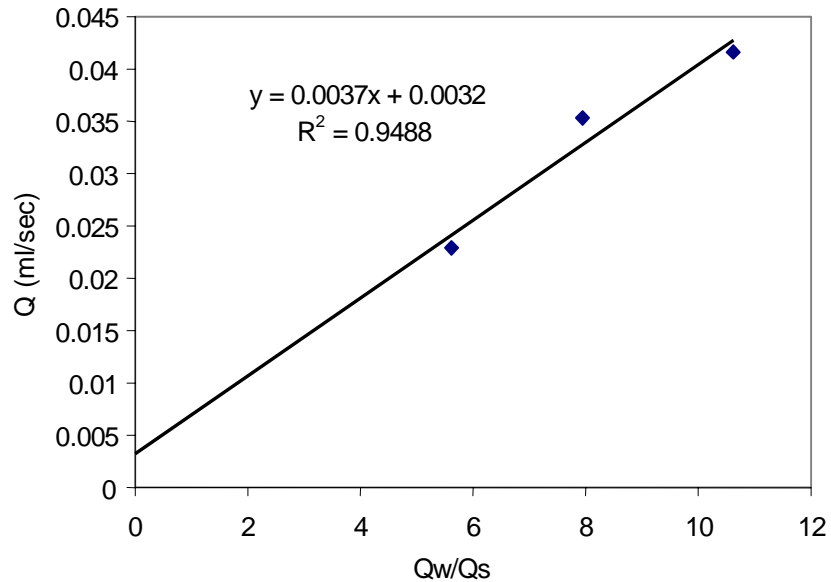

Figure 1.10: Q vs. Qw/Qs to infer Q* for the steam-water experiment of Chen et al. (2003).
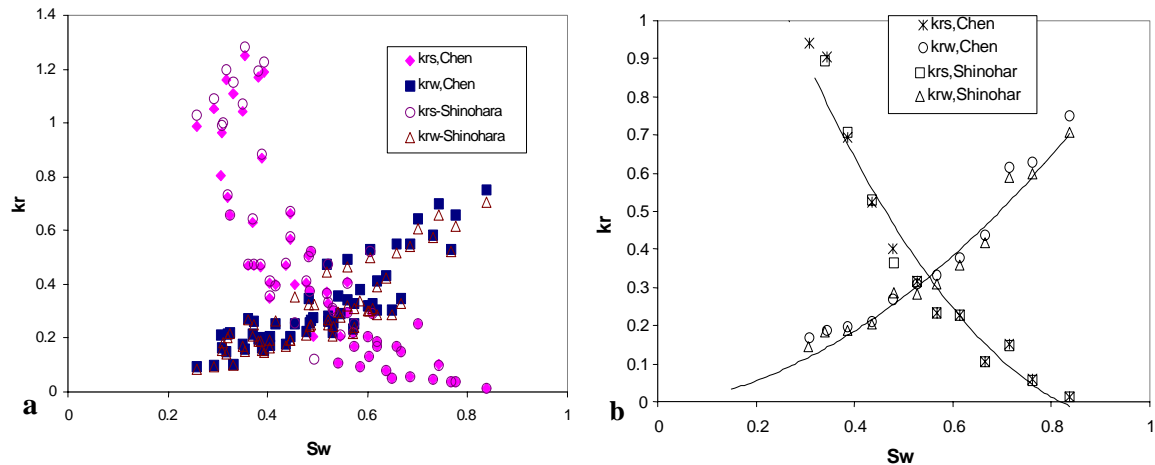

Figure 1.11: Comparison of steam-water relative permeabilities from porous media approach and Shinohara's method for the steam-water experiments: (a) generalized from experimental runs; (b) averaged values.
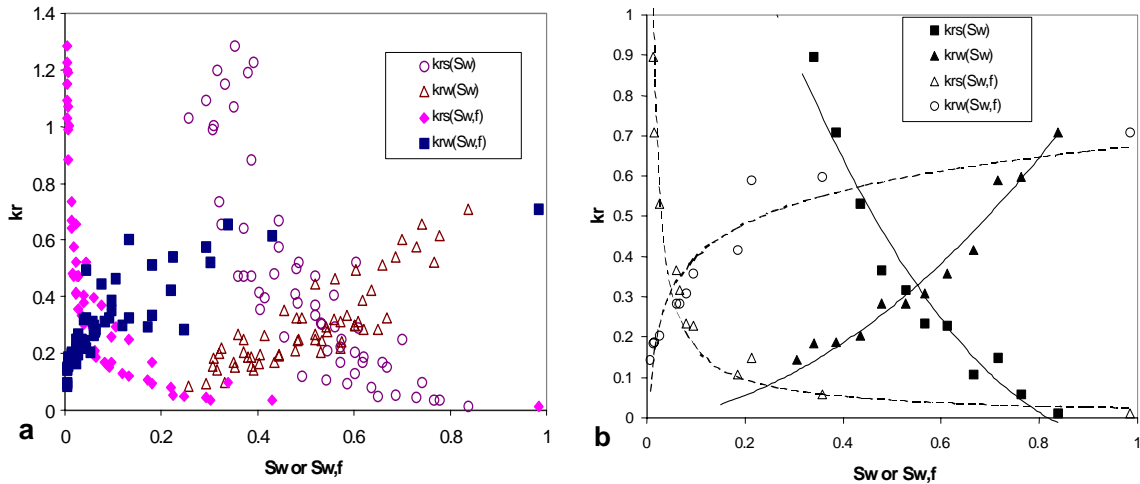
Figure 1.12: Comparison of kr vs. S_w and kr vs. $S_{w,f}$ from Shinohara's method for the steam-water experiments: (a) generalized from experimental runs; (b) averaged values.
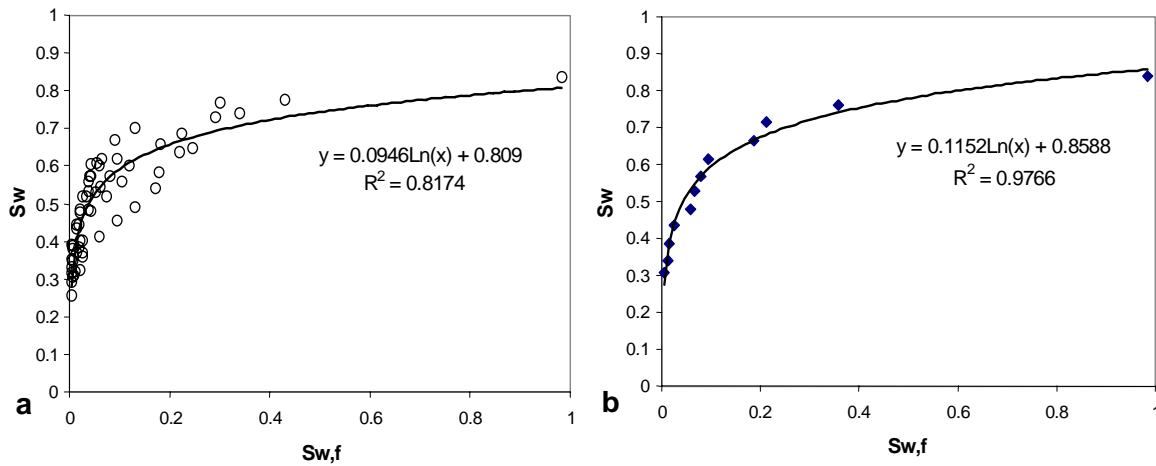

Figure 1.13: The flowing water saturation versus actual (static) water saturation: (a) generalized from experimental runs; (b) averaged values.

From Figures 1.11, 1.12 and 1.13, Shinohara's method can been demonstrated to obtain accurate relative permeabilities if the reservoir pressure gradient is close to constant. However, the flowing saturation values inferred from Equation 1.13 are a significant underestimate of the static (in-place) saturation. The difference between the two saturations is due to the velocity differences between steam and water phases, to the effects of immobile phases, and to the phase transformation effects. Therefore, we cannot simply use the flowing saturation to substitute for the real reservoir saturation. Figure 1.13b provides a mapping equation to relate the flowing and the actual water saturations for the laboratory scale measurements. The relationship between $S_{w,f}$ and S_w can be expressed as:

$$S_w = 0.1152\ln(S_{w,f}) + 0.8588 \tag{1.14}$$

By applying Equation 1.14 to convert the (flowing) water saturation values estimated from both the Geysers and Salton Sea production data, Figure 1.7 can be replotted against the corrected (static) water saturation, as shown in Figure 1.14. Comparing Figure 1.14 with

Figure 1.7, the underestimated water saturation has been improved, and Figure 1.14 shows more conventional relative permeability behavior. The relative permeabilities previously spanning from 0 to 0.23 (flowing) water saturation now range from 0 to 0.7 (static) water saturation after applying Equation 1.14. The solid curves in Figure 1.14 show the approximate trends of the relative permeability values for The Geysers and Salton Sea data, whereas the dashed lines are the trends for the experiments of Chen et al. (2003) shown earlier in Figure 1.13b. The estimates from the field production data still lie between the Corey and X-curves, and they are lower than the values measured by Chen et al. (2003). This observation may imply more phase interference in the actual geothermal reservoirs, which is reasonable. Greater phase interference may be attributed to several issues. First of all, the fracture and matrix interaction was not included in Chen et al.'s single fracture apparatus. The surface morphology, the complexity of nature fracture network, and the wettability difference of the materials were not considered in the smooth-walled fracture model of Chen et al. (2003). Moreover, the scale difference may be important too. Nonetheless, the similarities between the two sets of curves are striking.
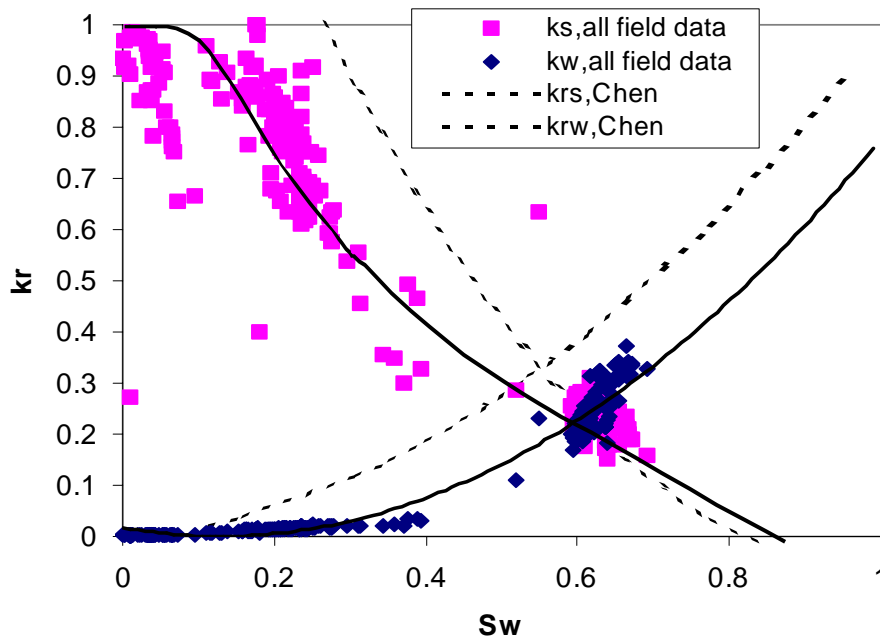

Figure 1.14: Relative permeability vs. mapped static water saturation from the field production data for The Geysers and Salton Sea Geothermal fields, compared to experimental results from Chen et al. (2003).

1.6 CONCLUSIONS

1) We can infer the steam and water relative permeabilities from field measurements of the production flow rate history and bottomhole temperature. Comparison with laboratory data demonstrated that this method can estimate the relative permeabilities accurately.

2) The estimated values of relative permeability in The Geysers and the Salton Sea geothermal fields lie between the X-curve and the Corey curve.

3) There is a sharp decline in the relative permeability of steam at small values of flowing water saturation, and this decline moderates as the saturation increases.

4) The relationship between the flowing water saturation and the actual (static) water saturation is close to logarithmic. After applying this correction, The k_r versus S_w curves from field data show a more conventional appearance.

5) In comparison to laboratory measurements from Chen et al. (2003), the estimated relative permeabilities from the field production data are lower, which implies that more phase interference occurs in the actual geothermal reservoirs.

2. THEORETICAL DEVELOPMENT OF THE BROOKS-COREY CAPILLARY PRESSURE MODEL FROM FRACTAL MODELING

This research project is being conducted by Senior Research Engineer Kewen Li. The objective is to derive the Brook-Corey capillary pressure model theoretically and study the effect of the error in estimating the residual wetting-phase saturation on the shape of a normalized capillary pressure curve.

2.1 SUMMARY

The capillary pressure model proposed empirically by Brooks and Corey (1964) has been used widely for several decades. However it is not clear why the Brooks-Corey capillary pressure model works so well. In this study, it has been found that the empirical Brooks-Corey capillary pressure model can be derived theoretically from fractal modeling. A correlation was found between the pore size distribution index in the Brooks-Corey capillary pressure model and the fractal dimension. The pore size distribution index increases with the decrease in fractal dimension of the porous media. Capillary pressure curves of different types of rock samples were measured using a mercury intrusion technique. The values of pore size distribution index and fractal dimension were calculated. The relationship between the two parameters obtained from the experimental data was consistent with the relationship derived theoretically. This implies that the fractal dimension of a porous medium may be inferred directly using the Brooks-Corey capillary pressure model. The theoretical development in this study demonstrates that the Brooks-Corey capillary pressure model, once considered as empirical, has a solid theoretical base. This may be why the Brooks-Corey capillary pressure model works satisfactorily in many cases.

2.2 INTRODUCTION

Capillary pressure plays an important role in steam production processes, so it is essential to represent capillary pressure curves properly. A model used frequently to express a capillary pressure curve mathematically is the Brooks-Corey model. Brooks and Corey (1964) conducted analysis for the capillary pressure curves of a large number of consolidated core samples. The capillary pressure curves were measured using a desorption approach. Brooks and Corey (1964) found that the relationship between the capillary pressure and the normalized or effective wetting-phase saturation was a straight line on a log-log plot. The mathematical expression of this relationship became known as the Brooks-Corey capillary pressure model. Residual wetting-phase saturation must be known or assumed to calculate the normalized or effective wetting-phase saturation. In the analysis by Brooks and Corey (1964), the residual wetting-phase saturation was chosen such that the data fit as closely as possible to a straight line when plotted on log-log paper.

The Brooks-Corey capillary pressure model works well in many cases and has been used widely for several decades in geothermal and other industries. However, given that it is an empirical model, it is not clear why the Brooks-Corey equation works so well.

Many researchers have studied the fractal nature of reservoir rocks and other porous media. It has been found that most natural porous media such as reservoir rock can be characterized using a fractal curve that represents the relationship between the number of pores and the radius of pores. Such a fractal curve is a straight line on a log-log plot and the slope of the straight line is referred to as the fractal dimension. The magnitude of the fractal dimension is a representation of the heterogeneity of the porous medium. The greater the fractal dimension, the greater the heterogeneity. Note that the pore size distribution index in the Brooks-Corey capillary pressure model is also a representation of the heterogeneity. The greater the pore size distribution index, the more homogeneous the porous medium.

In this study, we conducted a theoretical development based on the fractal geometry to derive the Brooks-Corey capillary pressure model. Capillary pressure curves of Berea, chalk, and reservoir sandstone were measured using a mercury intrusion technique to infer the fractal dimension. The values of fractal dimension were calculated using the fractal model and the Brooks-Corey capillary pressure model respectively and the results were compared.

2.3 THEORY

Previously Li (2004) obtained a relationship between the derivative of mercury (nonwetting phase) saturation and the capillary pressure using the theory of fractal geometry. The relationship is expressed as follows:

$$\frac{dS_{Hg}}{dP_c} = aP_c^{-(3-D_f)} \tag{2.1}$$

where a is a constant, S_{Hg} is the mercury (nonwetting phase) saturation, P_c is the capillary pressure, and D_f is the fractal dimension of the porous media.

If a three-dimensional pore model, instead of a two-dimensional capillary tube model, is used to calculate the number of pores, the following equation can be obtained (Li, 2004):

$$\frac{dS_{Hg}}{dP_c} = aP_c^{-(4-D_f)} \tag{2.2}$$

Eq. 2.2 was also derived by Friesen and Mikula (1987) using a different approach. Eq. 2.2 can be represented in a more general form in terms of the nonwetting phase saturation, S_{nw}:

$$\frac{dS_{nw}}{dP_c} = aP_c^{-(4-D_f)} \tag{2.3}$$

Assuming that P_c approaches to p_e when $S_{nw} = 0$, integrate Eq. 2.3:

16

$$\int_0^{1-S_w} dS_{nw} = a \int_{p_e}^{P_c} P_c^{-(4-D_f)} dP_c \qquad (2.4)$$

where S_w is the saturation of the wetting phase and p_e is the entry capillary pressure. According to Eq. 2.4, one can obtain:

$$1 - S_w = b[P_c^{-(3-D_f)} - p_e^{-(3-D_f)}] \qquad (2.5)$$

where b is another constant. Assuming that P_c approaches infinity when $S_{nw} = 1 - S_{wr}$, one can obtain according to Eq. 2.5:

$$1 - S_{wr} = -bp_e^{-(3-D_f)} \qquad (2.6)$$

where S_{wr} is the residual saturation of the wetting phase.

It is assumed that fractal dimension D_f is less than 3 in deriving Eq. 2.6 from Eq. 2.5. Combining Eqs. 2.5 and 2.6:

$$\frac{1 - S_w}{1 - S_{wr}} = 1 - (\frac{P_c}{p_e})^{-(3-D_f)} \qquad (2.7)$$

Arranging Eq. 2.7, one can obtain:

$$P_c = p_e(S_w^*)^{-\frac{1}{\lambda}} \qquad (2.8)$$

here S_w^* is the normalized saturation of the wetting phase and is expressed as follows:

$$S_w^* = \frac{S_w - S_{wr}}{1 - S_{wr}} \qquad (2.9)$$

and $\lambda = 3 - D_f$.

Eq. 2.8 is the frequently-used capillary pressure model proposed empirically by Brooks and Corey (1964).

One can see from the derivation of Eq. 2.8 that the Brooks-Corey capillary pressure model has a solid theoretical basis. This may explain why this model has been found to be suitable for many types of rock, including reservoir and artificial core samples.

The theoretical model shows that the pore size distribution index increases with the decrease in fractal dimension ($\lambda = 3 - D_f$). This is reasonable because porous media with greater heterogeneity have smaller values of pore size distribution index.

Note that the assumptions to derive Eq. 2.8 are: (1) fractal dimension D_f is less than 3; (2) P_c approaches infinity when $S_{nw} = 1 - S_{wr}$. The two assumptions are also the constraints to use the Brooks-Corey capillary pressure model.

Eq. 2.8 foresees that the relationship between the capillary pressure and the normalized saturation of the wetting phase is linear on a log-log plot. This is true in many cases. However the accurate estimation of the residual wetting-phase saturation (S_{wr}) is important to obtain such a straight line from the capillary pressure data measured by a mercury intrusion approach. Overestimation and underestimation of the residual wetting-phase saturation may change the linear relationship on a log-log plot. This will be discussed later in more detail.

2.4 EXPERIMENTAL MEASUREMENTS

Capillary pressure curves of different rock samples (sandstone and chalk) were measured using a mercury intrusion approach to obtain the fractal dimension.

The porosity of the Berea sandstone sample was about 23% and the air permeability was 804 md. The Berea sandstone sample used in this study was the same as that used by Li and Horne (2003). The porosity of the chalk sample was about 29.3% and the air permeability was about 0.17 md. The porosity of the reservoir sandstone sample was about 27.1% and the air permeability was about 2131 md.

The surface tension of air/mercury is 480 mN/m and the contact angle through the mercury phase is 140º according to the results reported by Purcell (1949).

2.5 RESULTS

The fractal dimension of a porous medium can be inferred from the capillary pressure curves using two methods (Eqs. 2.3 and 2.8). The values of fractal dimension calculated using Eq. 2.3 should be equal to those calculated using Eq. 2.8. To verify this, both theoretical and experimental capillary pressure curves were used in this study. The results are presented and analyzed in this section. Also discussed is the effect of the estimated residual wetting-phase saturation on the shape of the normalized capillary pressure curves.

Theoretical capillary pressure curves were calculated using different values of pore size distribution index, λ, to demonstrate the relationship between the fractal dimension and λ. Fig. 2.1 shows the capillary pressure curves calculated using the Brooks-Corey model (Eq. 2.8) with different values of λ. For simplicity, the residual wetting-phase saturation was fixed at 20% and the entry capillary pressure was fixed at 0.4 atm for all of the curves shown in Fig. 2.1. The values of λ ranged from 0.3 to 1.9. Fractal dimension can be inferred from the values of λ ($D_f = 3 - \lambda$).
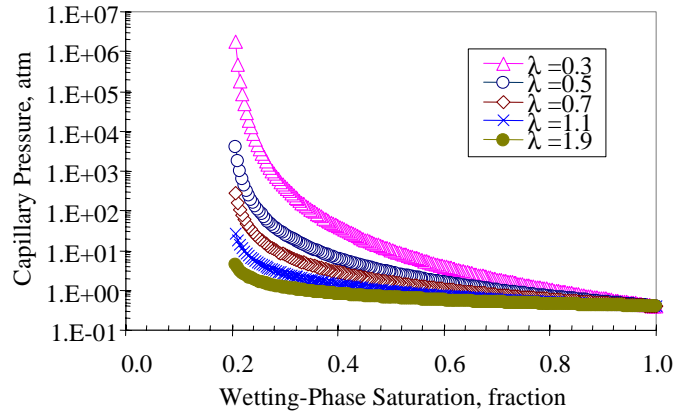
Figure 2.1:   *Capillary pressure curves with different values of pore size distribution index.*

The normalized wetting-phase saturations were calculated according to Eq. 2.9 and the relationships between capillary pressure and the normalized wetting-phase saturation are shown in Fig. 2.2. All of the relationships are straight lines, as expected.
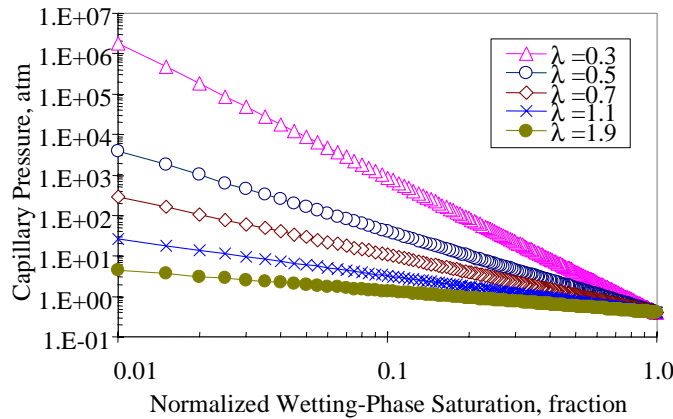

Figure 2.2:   *Normalized theoretical capillary pressure curves with different values of pore size distribution index.*

According to Eq. 2.3, the fractal dimension can be calculated once the relationship between capillary pressure and nonwetting-phase saturation gradient to the capillary pressure (dS_{nw}/dP_c) is known. The values of dS_{nw}/dP_c were calculated using the capillary pressure data shown in Fig. 2.1. The curves representing the relationship between dS_{nw}/dP_c and capillary pressure are shown in Fig. 2.3. All of the correlations are linear as foreseen in Eq. 2.3. The values of fractal dimension were calculated using Eq. 2.3 and were also inferred from the values of λ ($D_f = 3 - \lambda$). The results were compared and are listed in Table 2.1.

One can see from Table 2.1 that the values of the fractal dimension inferred from the relationship between dS_{nw}/dP_c and capillary pressure (using Eq. 2.3) are very close to those calculated from the value of λ ($D_f = 3 - \lambda$).

Table 2.1: Fractal dimension calculated using different methods.

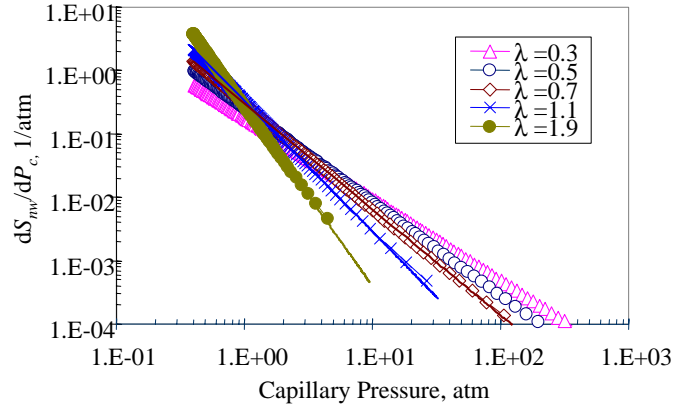|	λ	0.3	0.5	0.7	1.1	1.9
	$3-\lambda$	2.7	2.5	2.3	1.9	1.1
D_f	Eq. 2.3	2.73	2.53	2.33	1.94	1.16

Figure 2.3:   Relationship between dS_{nw}/dP_c and capillary pressure for different values of pore size distribution index.

To further demonstrate the relationship between the fractal dimension and the pore size distribution index, experimental capillary pressure curves were used. Fig. 2.4 shows the capillary pressure curves measured by using a mercury intrusion technique for different rock samples (Berea sandstone, chalk, and reservoir sandstone). The capillary pressure curves are different because the rock type and properties are different. Fig. 2.5 shows the corresponding normalized capillary pressure curves. Straight lines were obtained on a log-log plot. The values of the pore size distribution index were then calculated using Eq. 2.8 and the results are listed in Table 2.2. The values of fractal dimension were also determined from the values of λ ($D_f = 3 - \lambda$).
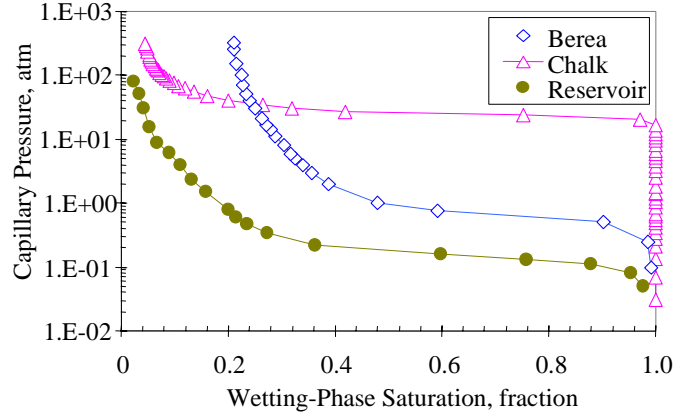
Figure 2.4:   Capillary pressure curves of different rocks (Berea sandstone, chalk, and reservoir rock).

Table 2.2: Fractal dimension and pore size distribution index calculated for different rock samples.

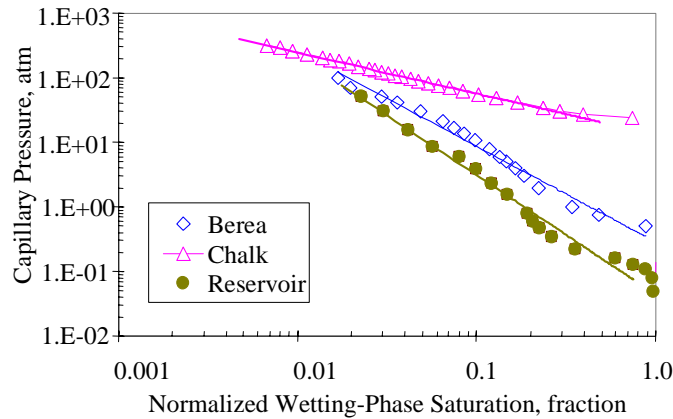| rock		Berea	Chalk	Reservoir rock
λ		0.674	1.572	0.542
D_f	$3-\lambda$	2.326	1.428	2.458
	Eq. 2.3	2.451	1.494	2.471

Figure 2.5:   Normalized capillary pressure curves of different rocks (Berea sandstone, chalk, and reservoir rock).

Fractal dimension can also be computed using the fractal model (Eq. 2.3) from the relationship between dS_{nw}/dP_c and capillary pressure. Fig. 2.6 shows the correlations between dS_{nw}/dP_c and capillary pressure of the three different rock samples. The values of the fractal dimension calculated using the data shown in Fig. 2.6 are listed in Table 2.2 and were compared with those inferred from the values of λ. One can see from Table 2.2 that

21

the values of the fractal dimension calculated using the two methods are almost the same for the samples studied.
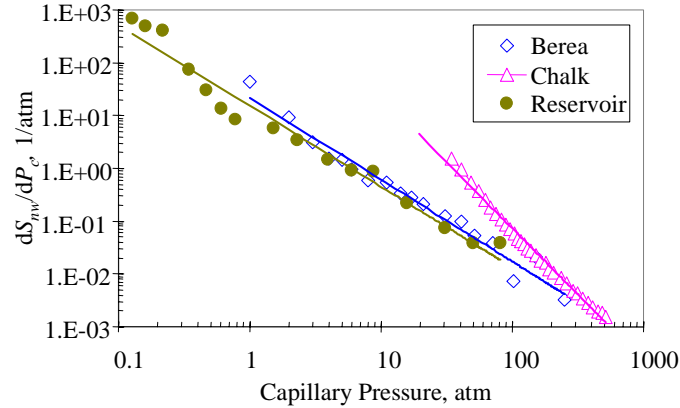

Figure 2.6:   Relationship between dS_{nw}/dP_c and capillary pressure for different rocks.

The calculations based on both the theoretical and experimental capillary pressure curves demonstrate that the fractal dimension may be inferred directly using the Brooks-Corey model instead of using the relationship between dS_{nw}/dP_c and capillary pressure. One advantage in determining the fractal dimension from the Brooks-Corey capillary pressure model is that there is no need to calculate dS_{nw}/dP_c.

As mentioned previously, accuracy in estimating the residual wetting-phase saturation is essential to obtain the linear relationship between the capillary pressure and the normalized wetting-phase saturation. Fig. 2.7 shows the effect of overestimation and underestimation of the residual wetting-phase saturation on the normalized capillary pressure curves for $\lambda=1.9$. The true value of the residual wetting-phase saturation was 20% in Fig. 2.7. The values of the normalized wetting-phase saturation were calculated using Eq. 2.9 with different values of the residual wetting-phase saturation (see the numbers close to each curve in Fig. 2.7). One can see that the normalized capillary pressure curve is linear only when the estimated value of the residual wetting-phase saturation is equal to the true value (20%). The normalized capillary pressure curve is concave to the horizontal axis if the residual wetting-phase saturation is overestimated. Otherwise the normalized capillary pressure curve is convex to the horizontal axis. One can see from Fig. 2.7 that the effect of the residual wetting-phase saturation on the shape of the normalized capillary pressure curves is significant.

Fig. 2.8 shows the effect of the estimated residual wetting-phase saturation on the shape of the normalized capillary pressure curves for $\lambda=0.3$. The phenomenon is similar to that shown in Fig. 2.7. However the effect of the estimated residual wetting-phase saturation on the normalized capillary pressure curves is more significant in the case with smaller value of λ than in the case with greater value of λ.
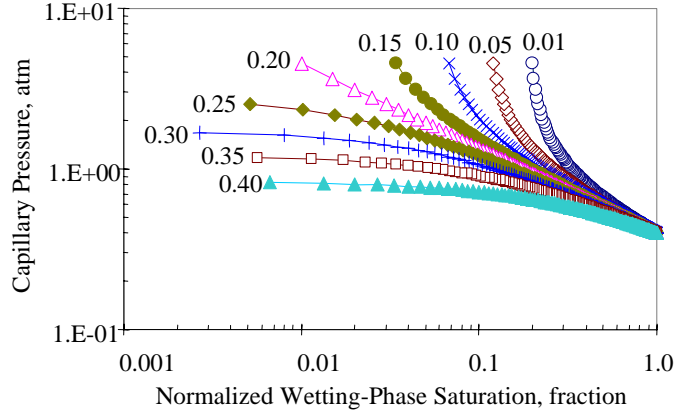
Figure 2.7:   Effect of residual wetting-phase saturation on the estimation of normalized capillary pressure curves ($\lambda=1.9$).
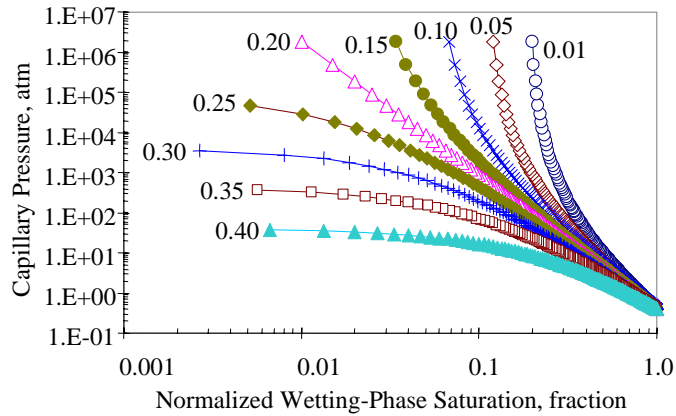

Figure 2.8:   Effect of residual wetting-phase saturation on the estimation of normalized capillary pressure curves ($\lambda=0.3$).

According to the results shown in Figs. 2.7 and 2.8, one can see that it is important to estimate the residual wetting-phase saturation accurately. Usually the true value of the residual wetting-phase saturation is smaller than the wetting-phase saturation at the maximum intrusion pressure during the mercury intrusion test. Brooks and Corey (1964) used the "trial and error" technique to choose the residual wetting-phase saturation. In this study, the solver function of Microsoft Excel was used to estimate the most appropriate value of residual wetting-phase saturation.

Note that if the normalized capillary pressure curve is concave to the axis, it does not always imply that the residual wetting-phase saturation is overestimated. For example, Li and Horne (2003) found that the capillary pressure curves of the rock from The Geysers geothermal field are concave to the axis of the normalized wetting-phase saturation. This is not brought about by the overestimation of the residual wetting-phase saturation because the normalized capillary pressure curves are still concave to the axis even if the residual wetting-phase saturation is set to zero

23

2.6 DISCUSSIONS

Although a theoretical basis of the Brooks-Corey capillary pressure model has been found, this does not imply that the model can apply in all cases without limitations. As mentioned previously, there are two known constraints to use the Brooks-Corey capillary pressure model. One of the constraints is that P_c approaches infinity when $S_{nw} = 1 - S_{wr}$. This may not be true in the case of imbibition capillary pressure curves. Another constraint is that the fractal dimension D_f is less than 3 (less than 2 if the capillary tube model is used). However the fractal dimension of the porous media with significant heterogeneity may be greater than this value. For example, Li and Horne (2003) found that the capillary pressure curves of the rock (with high density microfractures) from The Geysers geothermal field could not be represented using the Brooks-Corey capillary pressure model (although it could still be represented by a fractal model).

2.7 CONCLUSIONS

Based on the present study, the following conclusions may be drawn:

The Brooks-Corey capillary pressure model can be derived theoretically based on fractal modeling of porous media. This shows that the Brooks-Corey capillary pressure model, once considered as empirical, has a solid theoretical basis.

The pore size distribution index (λ) in the Brooks-Corey capillary pressure model increases with a decrease in fractal dimension (D_f) of the porous medium.

The fractal dimension of a porous medium may be inferred directly using the Brooks-Corey capillary pressure model instead of the fractal model in many cases.

Underestimation of the residual wetting-phase saturation may change the shape of the normalized capillary pressure curve from linear to nonlinear (convex to the axis of the normalized wetting-phase saturation) on a log-log plot.

Overestimation of the residual wetting-phase saturation may also change the shape of the normalized capillary pressure curve from linear to nonlinear (concave to the axis of the normalized wetting-phase saturation) on a log-log plot.

3. FRACTURED ROCK RELATIVE PERMEABILITY

This project is being conducted by Research Assistant Anson L. Villaluz, Senior Research Engineer Kewen Li and Prof. Roland N. Horne. The objective is to obtain measurements of steam-water relative permeability in real fractured rocks from geothermal reservoirs. This work is an extension of our earlier steam-water relative permeability studies, which have mostly considered artificially uniform and high permeability rocks. Now that the relative permeability mechanisms have been understood, we are ready to embark on the more difficult measurements using heterogeneous, low permeability rocks from geothermal reservoirs.

3.1 BACKGROUND

Steam-water relative permeability and capillary pressure are important for geothermal reservoir engineering calculations. In earlier studies, we have succeeded in making fundamental measurements of steam-water flow in porous media. One of the important problems left to undertake is the measurement of steam-water relative permeability and capillary pressure in actual geothermal rock (most of the previous study was conducted in high permeability sandstone as a well-controlled test material).

Using our existing steady-state CT method, we have measured steam-water relative permeability and capillary pressure in rock with permeability above 1 md (10^{-13} cm^2). We can obtain the in-situ fluid saturation simultaneously. For the geothermal rock with permeability smaller than 1 md (10^{-13} cm^2), the steady-state CT method would work but it would take an extremely long time to conduct the experiments (weeks or even months). Hence the CT method is not practical for geothermal rocks.

To overcome this difficulty, we have embarked on different approach, by measuring the relative permeability curves in separate sections. We have concluded from our experimental data (Satik, 1998; Horne *et al.*, 2000; Mahiya, 1999; O'Connor, 2001; Li and Horne, 2000a) that steam-water relative permeability follows the Corey model and steam-water capillary pressure follow the Brooks-Corey model. We can measure the end-point steam-water relative permeability and saturation in the geothermal rock with permeability smaller than 1 md using our existing steady-state CT method or the direct weighing method developed by Li *et al.* (2001). Then the whole curve of steam-water relative permeability can be obtained using the Corey model and the capillary pressure curve can be obtained using the Brooks-Corey model. We plan to confirm the applicability of this approach first with nitrogen-water experiments, which are much easier to conduct than the steam-water flows. This work was begun by Habana (2002), but ran into experimental difficulties.

The experimental study performed by Habana (2002) on a real fractured geothermal core resulted in measurements with pressure spikes occurring periodically during single-phase water injection. Erratic pressure spikes were also observed during nitrogen-water relative permeability experiment in the same study. Some of the results are presented in Figures 3.1 and 3.2. The appearance of these transient effects indicated a difficulty with the experimental configuration, and prevented the measurement of relative permeability. In

the continuation of this study, the apparatus has been redesigned and reconstructed to overcome these problems.
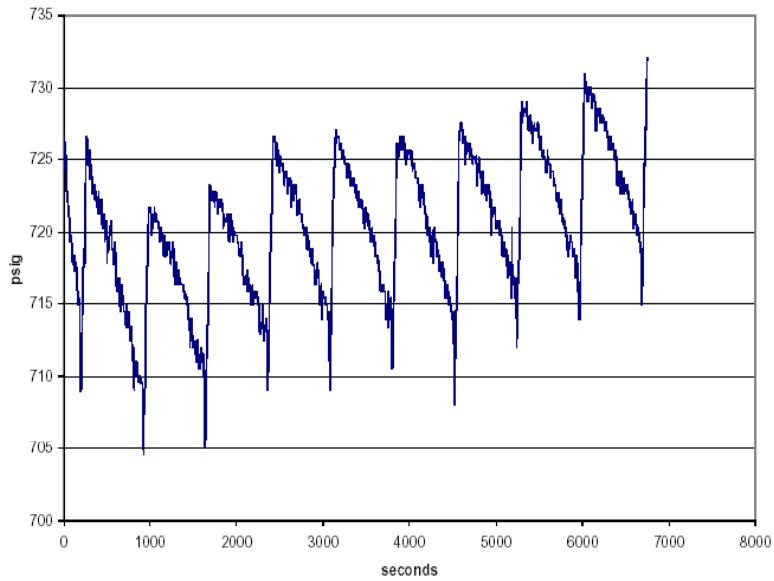

Figure 3.1: Pressure at inlet during water injection. Constant water flow rate at 14 ml/min (Habana, 2002).
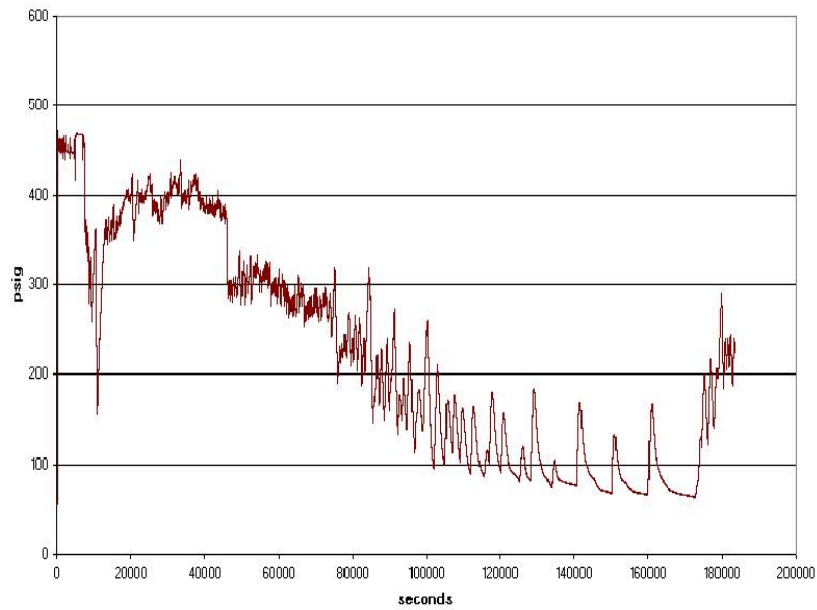

Figure 3.2: Pressure at inlet for constant flow rate nitrogen-water experiment (Habana, 2002).

3.2 EXPERIMENTAL METHODOLOGY

The rock permeability will be measured using nitrogen gas at room temperature. Gas permeability is a function of pressure, so the flow measurements will be conducted at a series of different mean pressures to take into account the Klinkenberg slip effect.

A new core sample has been obtained from a depth of 2440.5m at The Geysers geothermal field. The core is 8.9 cm in length and 4 cm in diameter.

Nitrogen will be flowed into the core at different confining pressures. Confining pressure from 500 to 850 psig can be reached by injecting nitrogen around the heat shrink tubing inside the core holder. To apply higher confining pressure water can be used in place of nitrogen.

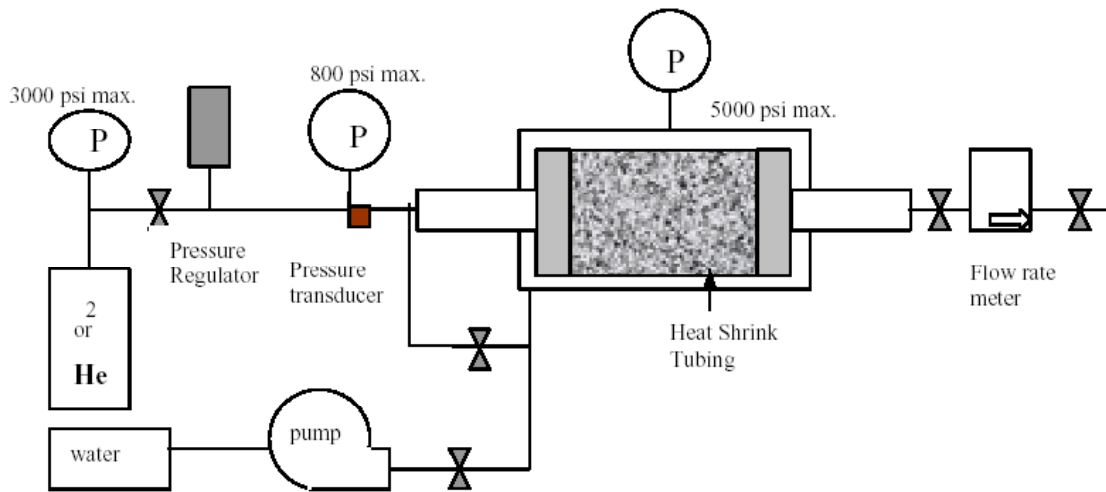A schematic illustration of the experiment is shown in Figure 3.3.

Figure 3.3: Schematic representation of apparatus.

In the current step, electrical resistivity was measured in a Berea sandstone to study the relationship of resistivity with saturation. Electrical resistivity measurement should be a more practical approach to measure saturation in a fractured rock compared to using the CT method or the direct weighing method. Figure 3.4 shows the core assembly.

The fully saturated core, together with the other parts were weighed while allowing water to naturally evaporate out of the core to investigate the applicability of Archie's equation.

Two sets of experiments were done, one using deionized water, the other employed 1% NaCl solution as the fluid saturating the sandstone.
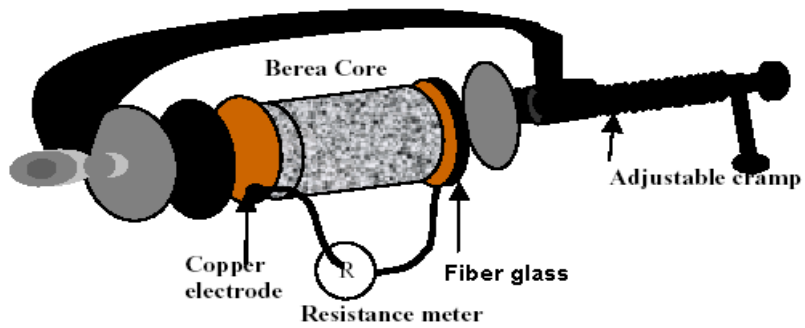
Figure 3.4: Diagram of core assembly used for electrical resistivity experiment.

3.3 THEORETICAL BACKGROUND FOR ELECTRICAL RESISTIVITY

The relationship between saturation and resistivity is given by Archie's equation. This relationship can be represented by the equation below:

$$I = bS_w^{-n} \tag{3.1}$$

where $I = R_t/R_o$ known as the resistivity index, R_t is the resistivity at a certain saturation, R_o is the resistivity at 100% water saturation, b is some function of tortuosity, and n is the saturation exponent. Empirically, $n = 2$ for Berea sandstone from previous studies.

3.4 RESULTS FOR THE ELECTRICAL RESISTIVITY EXPERIMENT

For the experiment using deionized water, the results are shown in Figure 3.5.
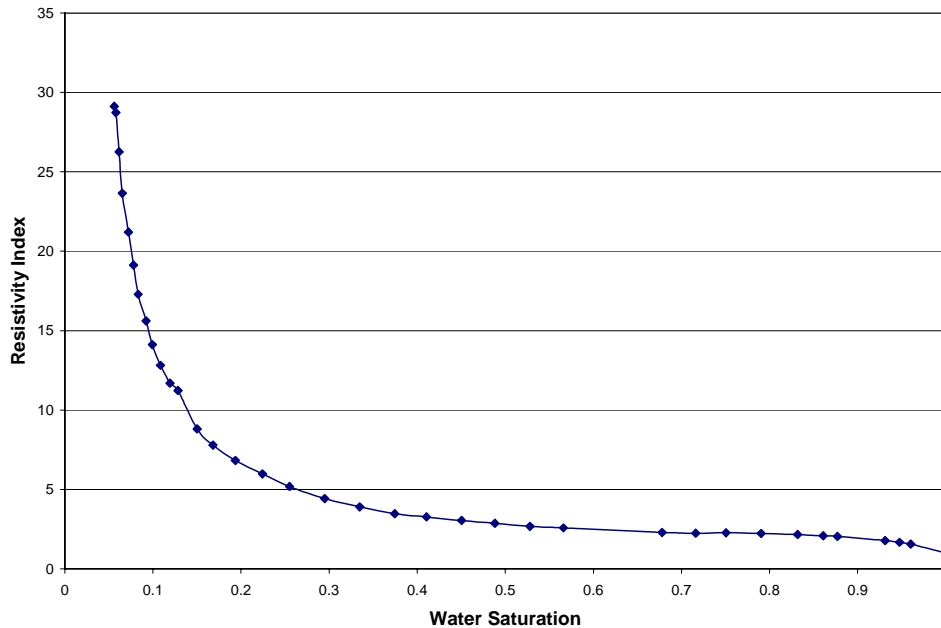

Figure 3.5: Saturation of Berea sandstone core versus Resistivity index (deionized water).
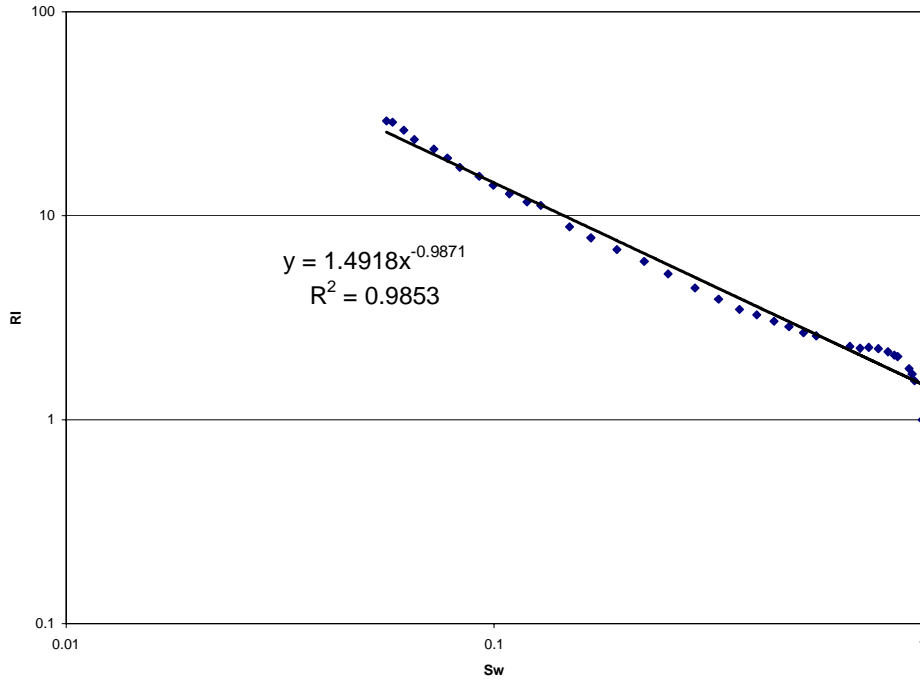
Figure 3.6: Archie's Correlation: Saturation versus Resistivity Index (deionized water).

Tthe results for the experiment using 1% NaCl solution are presented in Figure 3.7.
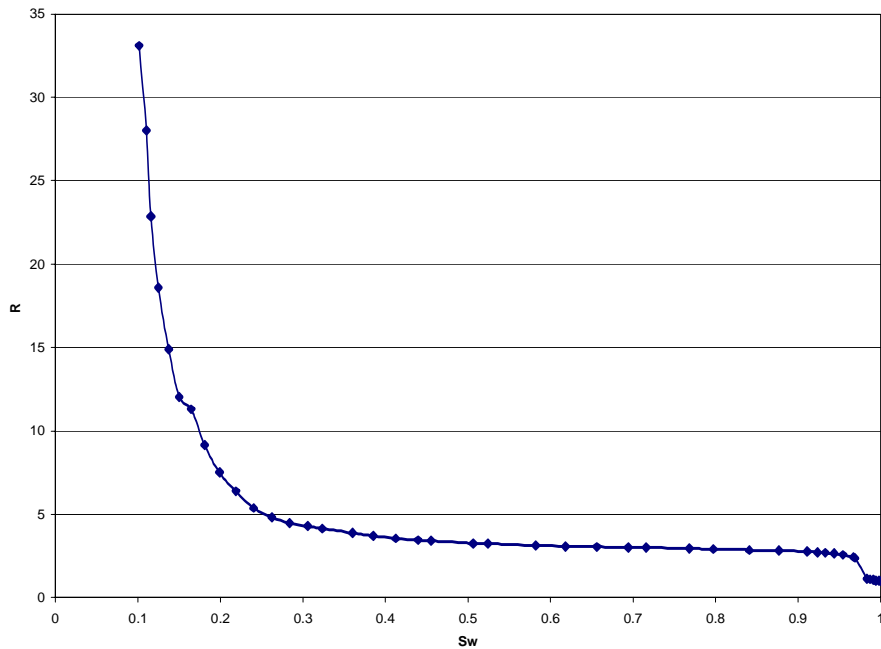

Figure 3.7: Saturation of Berea sandstone core versus Resistivity index (1% NaCl solution).
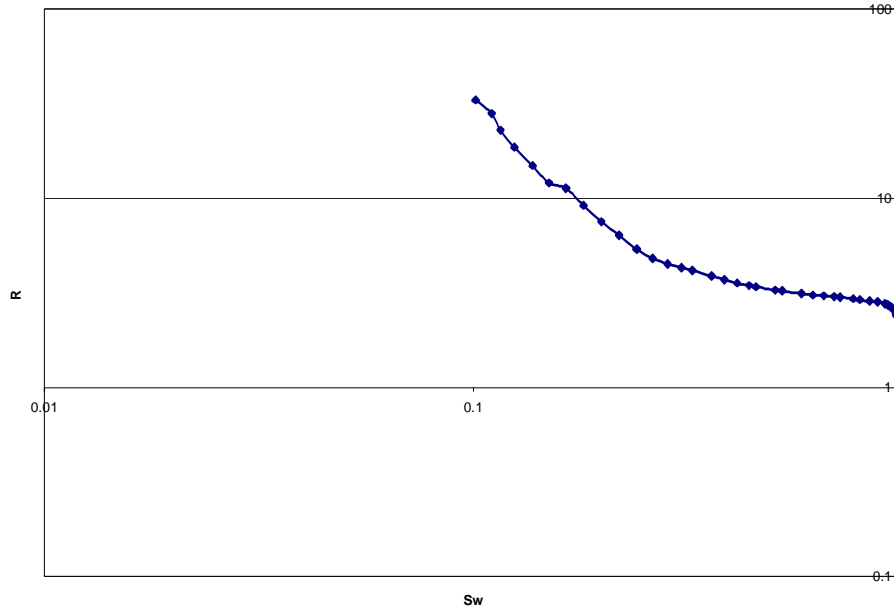
Figure 3.8: Archie's Correlation: using 1% NaCl solution.

As can be observed in Figures 3.5 and 3.7, resistivity is sensitive to saturation changes within the core. From these figures, it can also be seen that "capillary pressure"-like curves were obtained for both experiment runs.

Meanwhile, Figure 3.6 shows a reasonable linear fit to Archie's correlation for the core saturated with deionized water. However, the *n* value obtained for the sandstone was small (i.e., 1) compared to findings of other researchers (i.e., 2). On the other hand, Figure 3.8 shows a poor fit to Archie's correlation for the core saturated with 1% NaCl solution. These errors are probably caused by inaccuracy of the resistance measuring device used (a common multimeter) which imposes direct current (DC) to measure resistance. The industry standard nowadays is using alternating current (AC) to provide more accurate measurements of resistance.

3.5 CONTINUING AND FUTURE WORK

An experimental apparatus for measuring nitrogen-water relative permeability (Fig. 3.9) is currently being used to measure gas (N_2) and liquid (water) permeabilities. After this, a resistance measuring device employing AC voltage will be connected to the apparatus and nitrogen-water relative permeability measurements will be performed. The steady-state method will be applied.

It will be interesting to look for a possible correlation between electrical resistivity, saturation, relative permeability, and capillary pressure. This will also be a very valuable experience needed for conducting relative permeability measurements of fractured rocks.

At a later stage, we will investigate the application of pore network modeling to derive the relative permeability curves of fractured rocks.
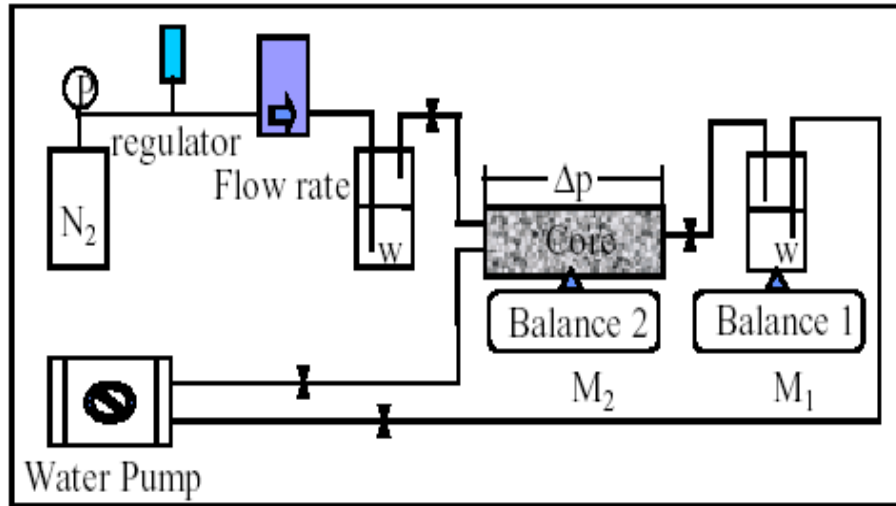

Figure 3.9: Schematic diagram of steady state N_2-H_2O relative permeability test.

4. REFERENCES

Brooks, R.H. and Corey, A.T.: "Hydraulic Properties of Porous Media," Colorado State University, Hydro paper No.5 (1964).

Chen, C.-Y., Diomampo, G., Li, K. and Horne, R.N.: "Steam-Water Relative Permeability in Fractures," *Geothermal Resources Council Transactions Vol.26*, pp. 87-94, 2002.

Chen, C.-Y., Li, K. and Horne, R.N.: "Difference Between Steam-Water and Air-Water Relative Permeabilities in Fractures," *Geothermal Resources Council Transactions Vol.27*, pp. 793-800, Oct., 2003.

Corey, A.T., 1954. "The Interrelations Between Gas and Oil Relative Permeabilities," *Producers Monthly, Vol. 19*, p. 38-41.

Diomampo, G., "Relative Permeability through Fractures", MS report, Stanford University, Stanford, California (2001).

Horne, R.H., Satik, C., Mahiya, G., Li, K., Ambusso, W., Tovar, R., Wang, C., and Nassori, H.: "Steam-Water Relative Permeability," Proc. of the World Geothermal Congress 2000, Kyushu-Tohoku, Japan, May 28-June 10, 2000.

Li, K. and Horne, R.N.: "Fractal Characterization of The Geysers Rock," presented at the Geothermal Resource Council 2003 annual meeting, October 12-15, 2003, Morelia, Mexico; GRC *Trans*. **27** (2003).

Li, K.: "Characterization of Rock Heterogeneity Using Fractal Geometry," SPE 86975, Proceedings of the 2004 SPE Western Region Meeting, Bakersfield, CA, USA, March 16-18, 2004.

Li, K. and Horne, R.N. (2000a): "Steam-Water Capillary Pressure," SPE 63224, presented at the 2000 SPE Annual Technical Conference and Exhibition, Dallas, TX, USA, October 1-4, 2000.

Li, K., Nassori, H., and Horne, R.N. (2001): "Experimental Study of Water Injection into Geothermal Reservoirs," to be presented at the GRC 2001 annual meeting, August 26-29, 2001, San Diego, USA; *GRC* Trans. V. **25**.

Mahiya, G.: "Experimental Measurement of Steam-Water Relative Permeability," MS report, Stanford University, Stanford, California (1999).

O'Connor, P.A.: "Constant-Pressure Measurement of Steam-Water Relative Permeability," MS report, Stanford University, Stanford, California (2001).

Purcell, W.R.: "Capillary Pressures-Their Measurement Using Mercury and the Calculation of Permeability", *Trans*. *AIME*, (1949), **186**, 39.

Shinohara, K., "Calculation and Use of Steam/Water Relative Permeabilities in Geothermal Reservoirs", MS report, Stanford University, Stanford, California (1978).

Satik, C.: "A Measurement of Steam-Water Relative Permeability," Proceedings of 23rd Workshop on Geothermal Reservoir Engineering, Stanford University, Stanford, California (1998).

Habana, M.D.: "Relative Permeability of Fractured Rock", MS report, Stanford University, Stanford, California, (2002).